Article:

Kearney, S.A., Tajuelo Rodriguez, E., Arregui-Mena, J.D. et al. (2 more authors) (2022) Simulation of radiation damage via alpha decay in BFS:PC grouts using 4He2+ ion acceleration. Cement and Concrete Research, 159. 106895. ISSN 0008-8846

https://doi.org/10.1016/j.cemconres.2022.106895

Cement and Concrete Research 159 (2022) 106895

Contents lists available at ScienceDirect

Cement and Concrete Research

journal homepage: www.elsevier.com/locate/cemconres

Simulation of radiation damage via alpha decay in BFS:PC grouts using $^{4}He^{2+}$ ion acceleration

Sarah A. Kearney [a], Elena Tajuelo Rodriguez [b], José David Arregui-Mena [b], Sebastian M. Lawson [a,c], John L. Provis [a,*]

[a] NucleUS Immobilisation Science Laboratory, Department of Materials Science and Engineering, University of Sheffield, Sheffield S1 3JD, United Kingdom
[b] Oak Ridge National Laboratory, Oak Ridge, Tennessee, United States of America
[c] GeoRoc International Ltd. and Gravitas Technologies Pty, Whitehaven, England, United Kingdom

ARTICLE INFO

Keywords:
Portland cement
Blast furnace slag
Alpha irradiation
Ion accelerator
Transmission electron microscopy

ABSTRACT

The impact of alpha radiation on cements used to encapsulate intermediate-level waste (ILW) is not well understood. ILW wastes can contain high levels of alpha-emitting radionuclides, meaning that the grouts used to encapsulate them are exposed to significant ionising radiation. Thus, a damaged region could develop in the grout adjacent to the alpha-emitting species. This work attempted to recreate this behaviour through nonradioactive $^{4}He^{2+}$ ion-accelerator experiments, which have not previously been applied to common encapsulation grouts. The influence of this irradiation on a slag-Portland cement was investigated at different ages via transmission electron microscopy energy-dispersive x-ray spectroscopy (TEM-EDX) and supporting techniques, to assess whether $^{4}He^{2+}$ irradiation caused textural or chemical zonation. No significant changes in hydrate phases or textures were observed, other than minor variations associated with carbonation. This paper provides a proof of concept for using ion acceleration techniques on cements and furthers knowledge on their radiation response.

1. Introduction

Managing non-heat-generating intermediate-level waste (ILW) via encapsulation in cementitious grouts is a common global practice. Cement provides both a physical and chemical barrier to prevent the release of radionuclides into the environment. However, ILW materials can contain radionuclides that emit radiation at levels >4 GBq/t alpha and >12 GBq/t beta/gamma, meaning the encapsulating grouts are exposed to high levels of ionising radiation throughout their service life. The radionuclides responsible for most alpha activity in ILW include Pu and U isotopes, which are present in fuel residues, and their associated decay products [1]. Current UK guidelines require waste-form properties to be maintained for 150 years post-manufacture, and the package forms a component of the multibarrier system employed by the geological disposal concept that aims to isolate waste for over 100,000 years [2]. Scientists must understand how radiation affects these materials so that a robust safety case for waste disposal can be developed.

The effects of alpha radiation on cementitious grouts are not well understood. The majority of irradiation studies focus on the potential of mechanical properties degradation for structural concrete in reactor environments and biological shielding in which neutron and gamma irradiation are the most pertinent. Studies tend to focus on Portland cement (PC), which is a component of structural concrete. The grouts used for encapsulation are commonly blends of PC with large proportions (>50 %) of supplementary cementitious materials, such as blast furnace slag (BFS), and thus have a distinct chemistry and microstructure. These changes will likely result in a different response to radiation compared with the more Ca-rich binders based on plain PC.

The impact of alpha radiation on cements will manifest via two processes: radiolysis and atomic displacements [3]. The radiolytic decomposition of pore fluid will generate gaseous products, reactive species, and overpressure, which could cause crack development. Due to the short path length of alpha particles within cements, these radiolysis reactions will occur in an extremely small volume surrounding each radiation source. This could create more molecular products, increasing gas production, and thus generate distinct chemical variations in the zone of influence of the radicals. Together with ballistic impacts from the alpha recoil and emitted particles, potentially causing amorphisation, these variations could produce damage zones similar to the radiohaloes observed in natural inclusions [4]. Most alpha studies are linked

---

* Corresponding author.
E-mail address: j.provis@sheffield.ac.uk (J.L. Provis).

https://doi.org/10.1016/j.cemconres.2022.106895
Received 6 November 2021; Accepted 26 June 2022
Available online 4 July 2022

to gas evolution, and data on microstructural impact are limited, but observations of the bulk have indicated that alpha encapsulation could be more likely to cause chipping and/or spallation and reduce strength than similar doses of gamma irradiation [5]. The impacts of these effects on the cement microstructure and any resulting changes in the physicochemical properties are currently unknown. More information is required on potential responsible mechanisms.

Previous work by the authors completed in collaboration with the UK National Nuclear Laboratory [6] investigated the bulk effects of the encapsulation of alpha-emitting radionuclides on the characteristics of PC-blended cements. The results of the x-ray diffraction (XRD) analysis in that study indicated potential changes to the phase assemblage in BFS-PC grouts as a result of chemically induced variations, leading to potentially expansive formation of sulfate-containing phases. However, only limited microstructural investigation of those samples was completed.

Therefore, the aim of this paper is to determine the impact of alpha decay on the microstructure of cementitious grouts used for nuclear waste encapsulation. Establishing whether ion acceleration provides an appropriate technique for simulating this in cementitious materials was a key objective, because the hydrated nature of the phase assemblage requires that care be taken to ensure that the experiment setup does not produce excessive sample heating. The influence of the radiolytic decomposition of pore fluid, which causes distinct zones of chemical variations, was also of interest because electronic stopping effects could cause significant chemical changes in the waste-form binder chemistry.

2. Experimental methods

2.1. Sample synthesis

Samples of 3.44:1 BFS:PC with a 0.35 w/s mass ratio were synthesised, because this formulation is common for ILW conditioning in the United Kingdom [7]. The precursor materials were Scunthorpe ground granulated BFS (BS EN 15167-1) blended with Calumite—a coarse ground material of the same composition—and Ketton CEM I 52.5N (BS EN 197-1) PC powders that conform to the Sellafield specification [7]. The oxide compositions of these materials are shown in Table 1.

Grouts were cured in sealed centrifuge tubes at 20 ± 2 °C until approximately 10 days before ion irradiation, when they were removed for preparation. Thin slices were taken from the monolith by using a slow saw and wafering blade. These were further thinned by using SiC grit papers, after which the sample surface was polished by using progressively finer cashmere cloths coated with diamond suspensions (6 μm decreasing to 0.25 μm). The application of organic solvents, for hydration arrest or for polishing, was avoided to minimise any interference in irradiation processes. After polishing, the dimensions of the cement samples were <15 mm in diameter and <1 mm thick. The densities of the samples were obtained by using an Archimedes balance, and averages of 1.90 and 2.03 ± 0.02 g cm^{-3} were observed for CEM4M (sample cured for 4 months) and CEM3Y (samples cured for 3 years), respectively, as shown in Table 2.

Table 1
Composition of raw materials determined by x-ray fluorescence (XRF) and represented as oxides.

Oxide	PC (wt%)	BFS (wt%)
SiO_2	21.6	36.1
Al_2O_3	5.1	11.4
Fe_2O_3	2.6	0.4
CaO	64.9	39.4
K_2O	0.8	0.7
MgO	1.0	8.4
Na_2O	0.2	0.4
TiO_2	0.4	0.9
Mn_2O_3	–	0.6
MnO	0.1	0.6
SO_3	2.6	–
S^{2-}	–	0.8
Cl^-	0.1	0.0

2.2. Ion irradiations

Irradiations were completed at the Helmholtz Zentrum Dresden Rossendorf Ion Beam Center by using 5 MeV He^{2+} ions to simulate alpha particle energies that replicate those of Pu and U decay products [8–10]. Sample and irradiation conditions are outlined in Table 2.

Irradiations were completed at room temperature, and samples were mounted on a water-cooled stage with C adhesive tape to reduce sample heating during exposure. The current density and flux were also kept low (Table 2) to minimise heating effects. Together with the consideration of the sample thermal conductivities (2.05 W/m·K), trials of the experimental setup using thermal-sensitive tapes indicated that approximate temperature variations of <1 °C would be achieved across the sample via this configuration. The ion beam angle of incidence was kept perpendicular to the sample surface throughout irradiation, with a scanning ion beam (spot size of 5 mm) moving in the *x* and *y* directions with a frequency of 1 kHz.

The damage induced in the sample via electronic and nuclear stopping was estimated with Stopping and Range of Ions in Matter (SRIM) [11] by using the “Detailed Calculation with Full Damage Cascades” option (SRIM 2013) operated with 99,999 ions. Given the variable composition of the material and the unknown proportion of elements and phases within the specific sample, displacement energies were set to 50 eV for all elements to allow damage to be estimated [12]. The damage-depth profile calculated from SRIM for the sample is shown in Fig. 1, which shows that these irradiation conditions are predicted to create a damage region that extends from the surface to approximately 5 μm with a peak damage of 4×10^{-3} displacements per atom (dpa) at a depth of 4.5 μm. The dpa is representative of, on average, every atom in a specific volume being displaced once for a given fluence. Electronic stopping (i.e., S_e) was observed to dominate energy loss, and maximum ratios of nuclear to electronic stopping (i.e., S_n/S_e) values of 9.5×10^{-4} were observed.

A fluence of 1×10^{15} ions/cm^2 was chosen as representative, based on testing completed on clay minerals that will form backfill materials or the near-field geological environment in geological disposal facilities, which used similar fluences [13,14]. Ion irradiation studies on other waste-form materials, such as ceramics, glass, and minerals [15,16] have also used similar fluences, so it was deemed appropriate to trial this experimental technique by using comparable testing parameters.

Estimates of the total absorbed alpha dose indicate that this fluence will provide a significantly higher dose than the dose previously observed by the authors for samples of similar compositions containing PuO_2 [6] in which the total absorbed dose was ~1 MGy at the characterisation age. The estimated dose from the aforementioned experimental setup is approximately 300 MGy, as calculated from Eq. (1) [13]:

Table 2
Details of samples and irradiation parameters.

Sample	Material	Age (years)	Ion type and energy	Current	Fluence (ions/cm^{-2})	Flux
CEM4M	3.44:1 BFS:PC	0.3	5 MeV He^{2+}	5 nA/cm^2	1×10^{15}	1.56×10^{10} He^{2+} ions/s/cm^2
CEM3Y	3.44:1 BFS:PC	3.3	5 MeV He^{2+}	5 nA/cm^2	1×10^{15}	1.56×10^{10} He^{2+} ions/s/cm^2

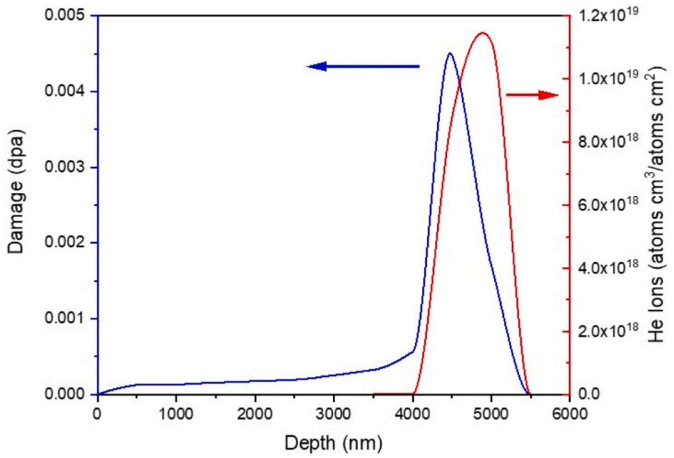

Fig. 1. Estimated displacement damage depth and ion density profiles for 3.44:1 BFS:PC cements irradiated with 5 MeV He^{2+} to a fluence of 1×10^{15} ions cm^{-2} calculated via SRIM [11].

$$D = \phi \cdot S \cdot m^{-1} \cdot 1.6 \times 10^{-19} \int_0^x \frac{dE}{dy} \cdot dy, \tag{1}$$

where D is the dose expressed in grays, ϕ is the fluence (ions/cm^2), S is the irradiated surface area (cm^2), dE/dy is the deposited energy (eV) per micron of range, x is the range (μm), and m is the mass (kg). Although this dose is far in excess of the dose experienced by the PuO_2-containing samples examined in previous alpha studies [6], it was considered to give the best test of experimental robustness and a conservative approximation of alpha irradiation tolerance.

2.3. Post irradiation characterisation

Characterisation was completed at the University of Sheffield (UoS) Materials for Innovative Disposition from Advanced Separations (MIDAS) facility via colour photography, scanning electron microscopy-energy-dispersive x-ray spectroscopy (SEM-EDX) (Appendix A), XRD, and Fourier transform infrared spectroscopy (FTIR).

Colour photography of the samples was conducted in a commercially available LED-lit lightbox with a Canon 4000D camera and was calibrated to a grey card of R/G/B 128/128/128. Average sample RGB values were extracted via ImageJ.

XRD analysis was performed on the ion implanted surface of monolithic samples, using a Bruker D2 Phaser with Cu Kα radiation and a Ni filter. Scans were completed between $5° < 2\theta < 70°$ with a step size of 0.02 °2θ and a dwell time of 2 s per step. Phase identification was performed using Diffrac.EVA V4.1 software with the ICDD PDF4 + 2015 database.

FTIR data were obtained by using a Perkin Elmer Frontier FTIR spectrometer equipped with a deuterated triglycine sulfate detector and KBr beam splitter optical system. Samples underwent scanning 16 times at a resolution of 4 cm^{-1} between 4000 and 400 cm^{-1}. Samples were prepared via the KBr pressed pellet method in which 2 mg of ground sample are mixed with 200 mg of KBr powder. Given this preparation and the small-damaged region (Fig. 1), the results unavoidably provide information on both the damaged zone and the bulk. Before measuring the samples, a background reading was taken to remove contributions from atmospheric CO_2 and water vapour.

The transmission electron microscopy (TEM)-EDX analysis was completed at Oak Ridge National Laboratory. To minimise differences between the samples in this comparative study, the same TEM sample preparation route was used to attempt to ensure that artefacts would not be mistaken for He^{2+} effects. SEM focused ion beam (FIB) sample preparation was conducted on an FEI Quanta 3D 200i Dual Beam instrument, which was used to produce lift-out irradiated sample specimens for TEM analysis. Upon locating a suitable area of the cement matrix, the stage was tilted to 52°, and a Pt strip was deposited to protect the surface. Trenches were cut adjacent to this by using a Ga beam with a current of 5–7 nA and an energy of 30 kV, after which the stage was tilted to 7°, and the lamella was undercut by using a reduced beam current of 3 nA. The lift-out needle was Pt welded to the lamella, and the remaining final cut was made to free the lamella and allow lift-out. The sample was mounted on a Cu TEM grid. The samples were thinned by using progressively lower beam currents (1, 0.5, 0.3, and 0.15 nA), and final cleaning was completed by using beam energies and currents of 5 and 2 kV and 48 and 43 pA, respectively.

TEM was completed by using a JEOL JEM-2100F TEM/scanning transmission electron microscopy (STEM) 200 keV field-emission system with Oxford X-Max 80 mm^2 Si drift detector EDX. Micrographs were captured in bright field (BF) mode using a CCD camera. Images were collected at a magnification of 20 kx by using spot size 1. For each sample, 30–50 EDX points were taken at 15 kx magnification by using spot size 1 and a beam diameter of 200 nm. To prevent shadowing effects during EDX acquisition, the stage was tilted to 20°, which also maximised x-ray collection and minimised spurious readings from thicker areas of the sample [17]. Compositional data from EDX analysis on unhydrated BFS within the samples were compared with the XRF results to allow calibration of the molar elemental ratios. Correction factors were calculated by using the method outlined by Prentice et al. [18] for the elemental ratios of BFS as shown in Table 3. The TEM lamella was mapped by using an FEI (now ThermoFisher) Talos F200X instrument in STEM mode operating at an acceleration voltage of 200 kV, which was used to characterize the TEM specimens. For this research, four images were captured simultaneously: BF, high-angle annular dark-field, and two types of intermediate annular dark fields named “DF2” and “DF4.” A Super-X energy dispersive spectrometer system coupled with the microscope was used to obtain the elemental compositions of the samples.

Selected area diffraction patterns were collected from areas that contain crystal clusters to ascertain the phases present, as well as from regions of C-S-H, to attempt to limit intermixing during chemical analysis. Crystalline phases were indexed by measuring the distance from the central point to the pairs of reflections in the diffraction pattern and by calculating the d-spacing via the camera length used to capture the image. The values were compared with standard crystallographic patterns to identify phases.

Although radiation damage is commonly investigated via high-resolution TEM in mineral and ceramic specimens to assess whether changes to the crystal lattice occurred [19–21], attempts to do this on cement samples have often led to the decomposition of the hydrate phases [22], so this was not completed as part of this work.

3. Results and discussion

3.1. Colour analysis

A visual inspection of the samples after irradiation indicated that a colour variation was caused by He^{2+} exposure, as shown in Fig. 2. The matrix appeared discoloured, and a yellow sheen was observed. This

Table 3
Comparison of BFS molar ratios obtained from XRF and TEM EDX data. Correction factors calculated from the calibration of the EDX data via the XRF values are displayed.

	Ca/Si	Al/Ca	Al/Si	Mg/Al	Mg/Ca	Mg/Si	S/Ca
XRF	1.09	0.29	0.31	0.74	0.21	0.23	0.02
EDX	0.96	0.40	0.39	0.82	0.33	0.32	0.09
Correction factor	1.13	0.71	0.81	0.91	0.65	0.73	0.21

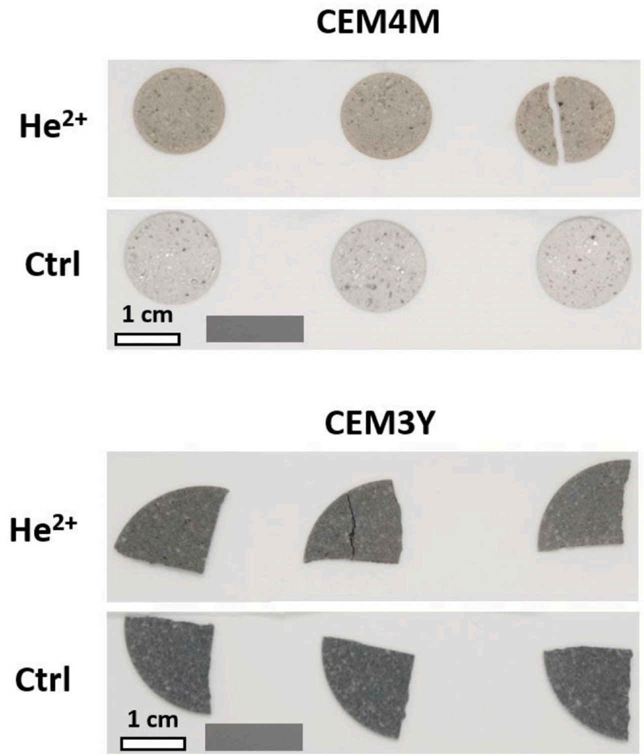

Fig. 2. CEM4M and CEM3Y after He^{2+} irradiation compared with the control samples showing colour variation. The reference grey card is shown at the base of the images. (For interpretation of the references to colour in this figure legend, the reader is referred to the web version of this article.)

effect was more pronounced in the younger CEM4M sample. Sections taken perpendicular to the irradiated face showed the discolouration to be a surface effect.

To quantify the difference between the samples, photographs were taken by using a grey card of a known RGB value, and an in-house methodology of colour measurement [23] was used to extract RGB values, allowing the mean values to be indexed, as shown in Table 4.

The variation in colour is similar to the discolouration effect observed in radiohaloes. Although these typically tend to be darkened rims adjacent to the alpha emitter, lighter yellow occurrences have been observed in cordierite ($Mg_2Al_4Si_5O_{18}$) [4,24]. The mechanism of the discolouration is not well defined. Although point defects were outlined as a potential cause of radiohaloes in biotite [25], there is debate regarding the impact of ionisation effects on their formation and the increased prevalence of these features within hydrated phases [4,19,24,26]. In hydrous materials, such as biotite, the radiolysis of OH^- groups has been linked to the reduction of Fe^{3+} from the metal-rich octahedral sheets, and the relocation of interlayer charge that balances species together with increased electron density has been attributed as a potential cause for sheets twisting or buckling, which leads to structural collapse [19,26].

Chaouche et al. [27] investigated the characteristic blue-green colour of BFS:PC and found that it was associated with the presence of a trisulfur radical ion, which is a blue chromophore. This could indicate that the colour change observed here is related to S redox changes, although typically a decrease in this species leads to bleaching to white rather than the yellowing observed in the samples in this investigation. The disulfur radical anion is a yellow chromophore [28]; however, the presence of this species was not detected by Chaouche et al. [27]. Also, the involvement of transition metals in the colouration of the cement was not considered as part of this study, although they might significantly contribute to colour together with the S chromophores.

Table 4
Indexed RGB values for irradiated and control CEM3Y samples.

Sample	CEM3Y	CEM3Y Ctrl	CEM4M	CEM4M Ctrl
RGB	115/114/110	97/100/100	171/163/150	205/201/196

Colour response in materials due to irradiation exposure is a well-documented phenomenon, and it is commonly used industrially to produce gemstones [29,30]. Altering $[AlO_4]^0$ colour centres forms “smoky” quartz, creating the characteristic darkening upon irradiation [31]. Lima and Lameiras [30] found that upon irradiation of quartz, the intensity of colour change was linked to the movement of charge-balancing Li^+ away from $[AlO_4]^0$ centres; this corresponds well with the loss of interlayer K^+ from He^{2+} irradiated biotite [14].

An analysis of the redox states of S and Fe is considered valuable for further work for these samples because assessing changes in oxidation states will help explain the mechanism of colour change.

3.2. XRD

XRD was completed on the polished surfaces of the ion-irradiated and control samples to allow comparison post-irradiation. The identified phase assemblage comprised calcium monosulfoaluminate (PDF# 83-1289), hydrotalcite (PDF# 14-0191), calcium monocarboaluminate (PDF# 36-0377), portlandite (PDF# 04-0733), vaterite (PDF# 33-0268), aragonite (PDF# 01-076-0606), and C-A-S-H, together with unreacted belite (dicalcium silicate, PDF# 29-0369) and BFS (identifiable from the diffuse scatter at 25°< 2θ <35°). A significant increase in carbonation was observed in CEM4M compared with CEM3Y, which was the result of atmospheric carbonation that could not be controlled as part of the ion irradiation setup. The difference pattern in Fig. 3A indicates that the control sample was more carbonated; this is likely due to the time spent under vacuum for the He^{2+} irradiated sample. A higher proportion of hydrotalcite was noted in CEM3Y, which is expected in samples of this advanced age because of increased BFS hydration [32,33].

Despite the carbonation effects in CEM4M, the difference patterns in Fig. 3A and B show that the diffraction patterns of these samples were very similar. No shift in peak position or width was observed, indicating that ballistic damage to the crystalline phases was limited, as anticipated from SRIM modelling. Although a weak reflection associated with vaterite was observed in the CEM3Y He^{2+} irradiated sample at 27.1 °2θ, no significant increase in carbonate products was observed. The consistency in the phase assemblage indicates that ionisation effects from the electronic stopping of the He^{2+} ions have not caused bulk changes to the crystalline components of the cement. The portlandite reflection at ~18° was stronger in the control CEM3Y sample than in the irradiated sample, whereas the reflection at ~34° was weaker. This makes the total intensity (i.e., area) for the portlandite phase similar for both samples, suggesting that carbonates do not form at the expense of this phase.

3.3. FTIR

The FTIR spectra of control and He^{2+} irradiated samples are shown in Fig. 4A and B, respectively. Overall, these data support the XRD findings; similar phase assemblages are identified in both samples. Increased carbonation was observed in CEM4M compared with CEM3Y, and the CEM4M control sample was more heavily carbonated than the He^{2+} irradiated sample.

However, the FTIR response from the CEM3Y He^{2+} irradiated sample shows the opposite response. Lower intensities between 900 and 1100 cm^{-1} indicate a decrease in the asymmetric stretching vibration in Si-O-Si, which here can be associated with Q^2 species in the C-S-H chains [34]. Increased resonances at 875 cm^{-1} and 1300–1600 cm^{-1} in the He^{2+} irradiated sample are associated with the out-of-plane deformation mode vibration and asymmetric stretching of CO_3^{2-}, respectively, indicating increased carbonate content [34]. The peak symmetry observed

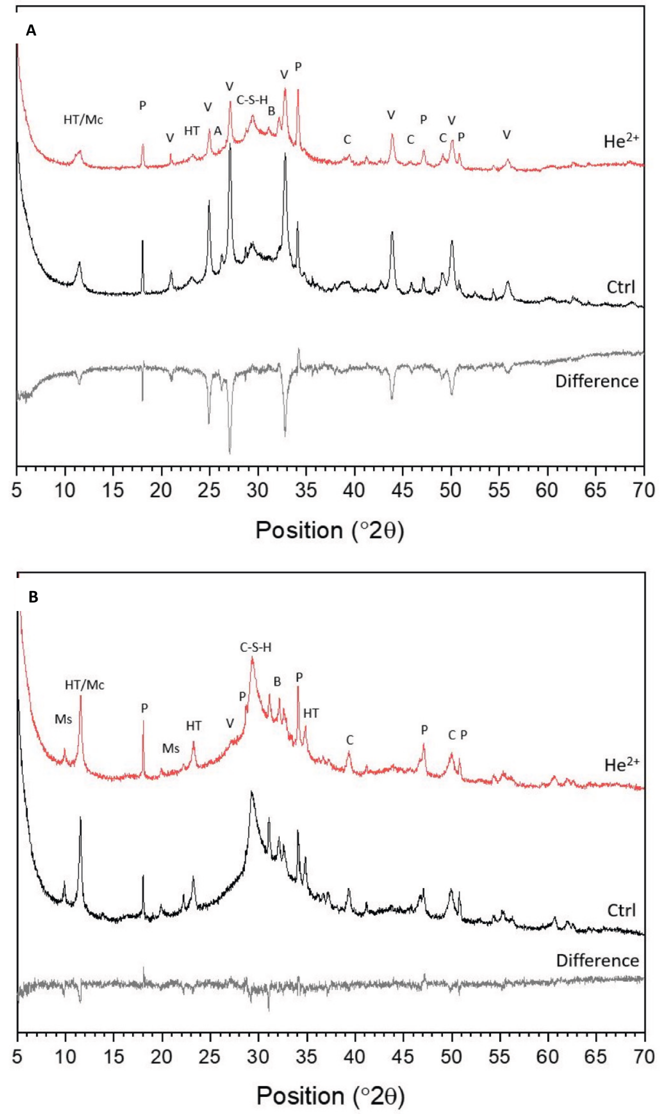

Fig. 3. XRD of He^{2+} irradiated (He^{2+}) and control (Ctrl) for (A) CEM4M samples and (B) CEM3Y samples. The difference pattern shows He^{2+}- Ctrl.

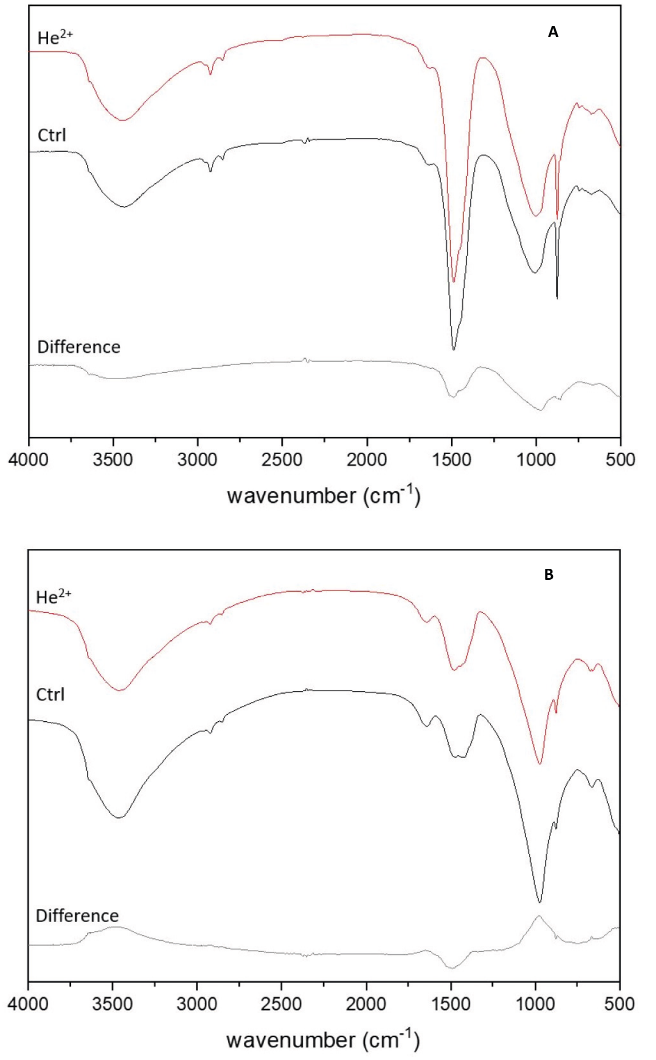

Fig. 4. FTIR spectra of (A) CEM4M He^{2+} irradiated (He^{2+}) and control (Ctrl) samples and (B) CEM3Y He^{2+} irradiated (He^{2+}) and control (Ctrl) samples. The difference pattern shows He^{2+} - Ctrl.

at 1300–1600 cm^{-1} shifts in the irradiated sample, indicating a difference in the polymorphs of $CaCO_3$ present; vaterite and aragonite peaks at 1485 cm^{-1} dominate over amorphous carbonates at 1425 cm^{-1} [35]. The reduction in response associated with the Q^2 species and increased carbonate content suggest that increased carbonation is proceeding at the expense of C-S-H, which is undergoing decalcification and becoming less polymerised. This also correlates with the observation of a similar portlandite intensity in the XRD data for control and irradiated samples. However, no peak shift is observed, which would be anticipated if the Ca/Si ratio had decreased significantly [34]. This minor variation supports the XRD results for the CEM3Y sample, which showed a small reflection associated with vaterite in the He^{2+} irradiated sample.

Regarding the mechanism of the increased carbonation, atmospheric effects cannot be discounted. However, the irradiated samples were stored under vacuum during testing and the control samples were not, which should minimise potential atmospheric effects. Thus, the potential for the radiolytically generated formation of metastable $CaO_2 \cdot 8H_2O$ facilitating carbonate production, as has been proposed in studies of PC [36–38], cannot be dismissed.

The peak located at 1640 cm^{-1} and the broad resonance centred at 3450 cm^{-1} are due to H-O-H bending vibrations in molecular H_2O and stretching vibrations of O-H bonds in H_2O or hydroxyls, respectively [34]. The slight peak reduction in the CEM3Y irradiated sample (Fig. 4B) at 1640 cm^{-1} indicates water loss through sample drying, and the reduced resonance at 3450 cm^{-1} shows a reduction in interlayer water molecules. This was not observed for the CEM4M sample (Fig. 4A). These minor effects are likely a product of drying due to the vacuum exposure because heating effects were minimised during testing. As the difference in FTIR response is small, the water variation is considered minimal.

3.4. TEM EDX

TEM micrographs were collected for the He^{2+} irradiated and control samples, allowing the C-S-H morphology to be investigated and potential chemical changes from irradiation to be more closely investigated. EDX point analysis data were collected. Overviews of the FIB samples are shown in Appendix A. Due to the multiphase nature of the sample, preparing a uniformly thick sample was impossible. Harder phases, such as unreacted BFS, could not be thinned to the same extent as the hydrate matrix, so thicker regions appear darker in the micrographs, and holes in the delicate C-S-H matrix developed in some regions.

Foil-like C-S-H morphologies were predominantly observed in CEM4M control samples (Fig. 5) with minor fibrillar-like zones noted

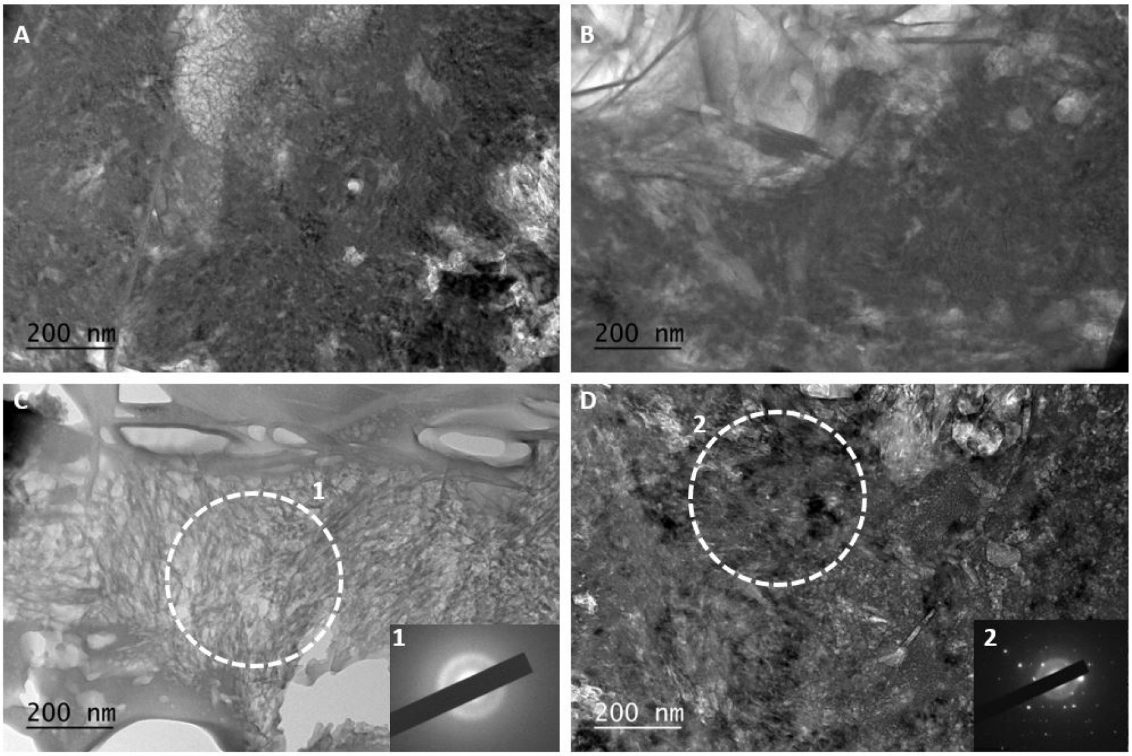

Fig. 5. TEM micrographs of CEM4M control. (A) Dense C-S-H foils with microcrystals. (B) C-S-H foils with microcrystals and lathes. (C) Open-textured foil-like C-S-H with zones of fibrillar C-S-H; the dashed circle represents the area of SAED pattern 1: C-S-H. (D) Dense foil-like C-S-H with microcrystals; the dashed circle represents the area of SAED pattern 2: portlandite.

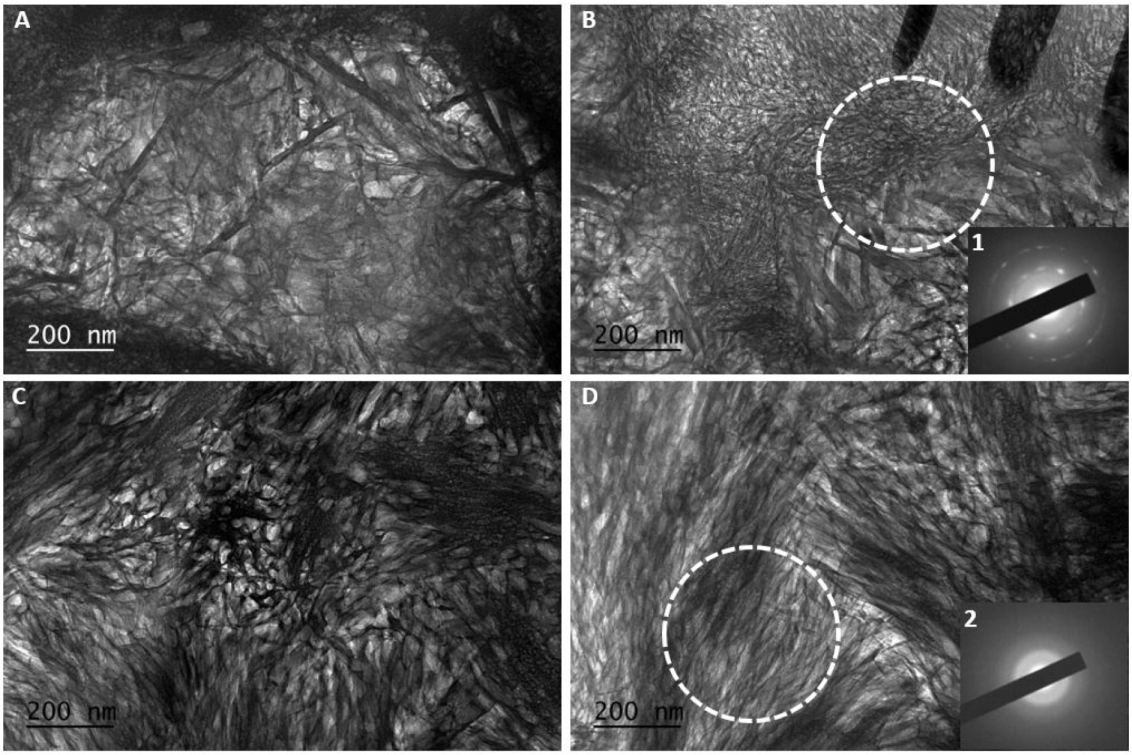

Fig. 6. TEM micrographs of CEM3Y Control. (A) Hydrotalcite laths observed. (B) Dense C-S-H foils with microcrystals and lathes; the dashed circle represents the area of SAED pattern 1: calcite. (C–D) Dense fibrillar C-S-H with zones of foil-like C-S-H; the dashed circle represents the area of SAED pattern 2: C-S-H.

(Fig. 5C). Dense microcrystals were observed throughout the matrix and identified as predominantly portlandite through selected area electron diffraction (SAED) indexing. Where microcrystals were observed, the matrix was dense with tight foil-like C-S-H (Fig. 5A, C, D), but more open-textured C-S-H was observed in areas without microcrystals. The differentiation between inner and outer product zones was observed (Fig. 5B), and minor areas of lath-like crystals were observed at the interface. Given the age of the samples and the XRD (Fig. 3A), which indicate that there was limited hydrotalcite in these samples, this is unsurprising.

Foil-like and fibrillar morphologies of C-S-H were observed in the matrix of the CEM3Y control sample. Fibrillar textures were identifiable by the strong linear directionality (Fig. 6D), which is not apparent in the more crumpled foil-like morphologies. The overall matrix texture was dense, and the C-S-H was predominantly foil-like, although a different foil coarseness was observed. For example, the tight, dense foils shown in the centre and top of Fig. 6B were compared with the more open, coarse textures shown intermixing with lath-shaped crystals in Fig. 6A. Space constraints during formation are likely responsible for these differences [39,40]. A clear distinction between the zones of the inner and outer product was not as defined as in the CEM3Y samples shown in Appendix A; Fig. A8. However, Fig. 6B shows the shift from the outer product in the top half of the image to areas more representative of the inner product in the bottom right and left corners. Given the age of the sample, the differences between the inner and outer product would be expected to decrease; as such, it is unsurprising that a clear distinction cannot be made throughout the sample or that different stages of microstructural development are present within the heterogeneous bulk [39].

Zones of microcrystalline calcite were observed within the C-S-H matrix (Fig. 6B), which were identified via SAED. However, attempts to collect diffraction data from the hydrotalcite laths were unsuccessful because the patterns were not strong enough for identification. The SAED pattern of C-S-H free from other hydrate products is shown in Fig. 6D.

High proportions of hydrotalcite laths were observed. However, as noted previously, the distribution of this phase was predominantly in inner product areas and adjacent to boundaries between the inner and outer product. Examination of similar 20-year-old cement formulations showed the distribution of hydrotalcite in areas tentatively thought to represent the outer product in terms of texture [33], and significant microstructural refinement is expected to occur as time and hydration progress. This is important because the impact of radiation on the system could be altered, depending on the microstructure, which could affect the performance of the material differently (e.g., in terms of creep behaviour [41]).

An analysis of the He^{2+} irradiated samples showed the same microstructural development as observed for the control samples. For CEM3Y He^{2+}, this included a dense C-S-H matrix of predominantly foil-like morphology with some fibrillar regions noted, zones of microcrystals within the matrix, and lath-like hydrotalcite found at textural boundaries. Similar observations were found for CEM4M He^{2+}, however; the C-S-H matrix was open-textured and foil-like with frequent microcrystals producing regions of denser microstructure. In both He^{2+}samples, the coarseness of the C-S-H foils was also variable, which was again considered to represent the inner and outer product regions due to space constraints during formation.

Fig. 7 shows micrographs of CEM4M at increasing depths from the irradiated surface. Although the sample is heterogeneous throughout, there were no identifiable systematic changes to the C-S-H morphologies as a function of depth that could be attributed to electronic stopping of the He^{2+} ions. The micrographs shown in Fig. 7A–D represent material from within 1 μm and >4 μm of the irradiated surface. Estimations of damage depth from SRIM (Fig. 1) indicate that peak damage should occur at approximately 4.5 μm. However, Fig. 7 shows no differences in terms of overall microstructure or, more specifically, C-S-H morphology;

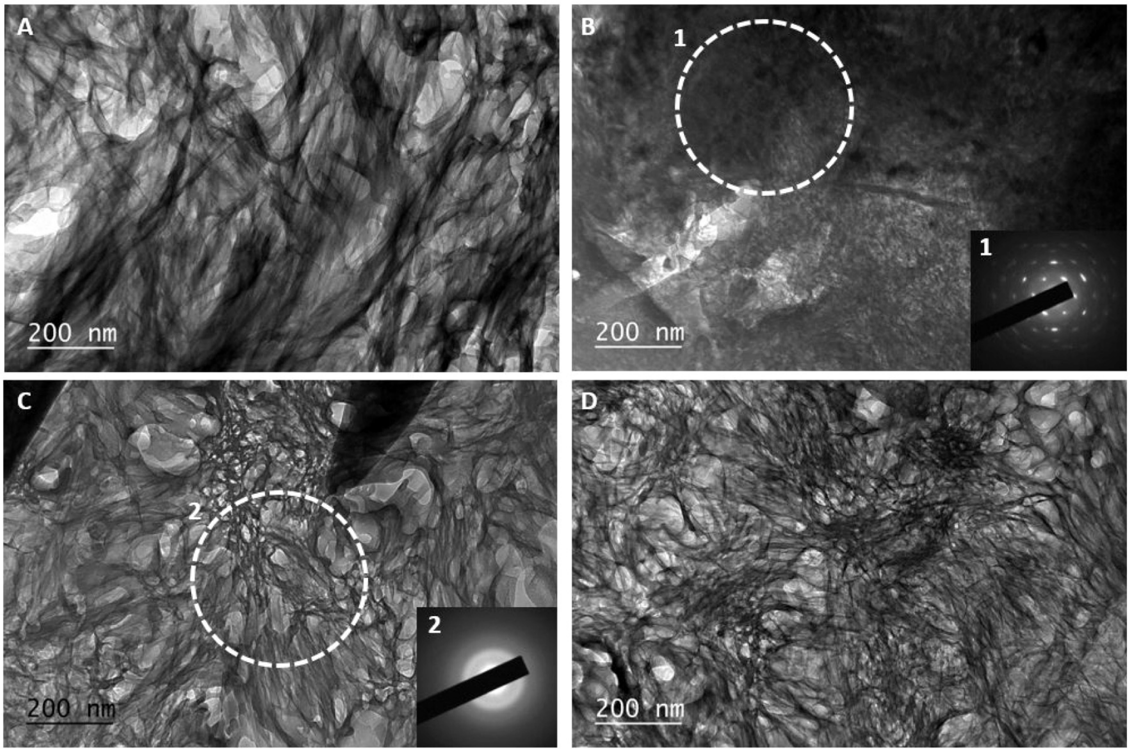

Fig. 7. TEM micrographs of CEM4M He^{2+} irradiated. (A) <1 μm from the irradiated surface with open, foil-like C-S-H with fibrillar zones. (B) Approximately 1.5 μm from the irradiated surface with dense C-S-H foils with microcrystals; the dashed circle represents the area of SAED pattern 1: portlandite. (C) 3 μm from the irradiated surface with open, foil-like C-S-H; the dashed circle represents the area of SAED pattern 1: C-S-H. (D) >4 μm from the irradiated surface with regions of open and dense foil-like C-S-H with zones of microcrystals.

open foil-like C-S-H with zones of dense microcrystals predominate throughout. Compared with the control sample, the FIB section was more stable during preparation; fewer holes in the matrix were formed, and more zones of C-S-H were observed as a result.

The images shown in Fig. 8 show regions of CEM3Y at increasing depths from the irradiated surface. The CEM4M images in Fig. 8A–D represent material from within 1 μm and >4 μm deep. As was observed in Fig. 7, the sample is heterogeneous throughout, but there were no identifiable systematic changes to the C-S-H morphologies as a function of depth. The presence of calcite microcrystals in the sample at greater depth was not distinctive because regions were also observed nearer the surface. The irradiation response of foil-like morphologies with varying coarseness was not observed to change because of He^{2+} exposure; no difference was observed.

Despite the overall similarities between the control and irradiated sample, there were regions in the CEM3Y He^{2+} irradiated sample in which the microstructure appeared to have lost its characteristic morphology; an example of this is shown in the bottom left corner of Fig. 8B. The globular appearance of the matrix in this region might be the product of variable sample thickness combined with cross sectioning through crumpled C-S-H foils [33], or it might be the product of beam damage from either the SEM-FIB preparation or TEM examination. However, areas of beam damage were observed in the control and irradiated samples that were considered more characteristic of FIB and TEM than these features. FIB damage is generally linear because of beam direction, so it tends to present as channels called *curtaining* in which Ga becomes embedded at the base [42,43] in some cases, and burning from TEM exposure leaves a circular rim, denoting the beam circumference within which the damage occurs [17].

Areas of similar featureless/globular microstructure were seen in the CEM3Y control sample. Unlike the sharp distinction seen in the CEM3Y He^{2+} sample (Fig. 8B), these texturally featureless zones in the control sample were pervasive across large areas with a gradual reintroduction of distinct morphologies. Given the current analysis and the complex nature of the hydrate morphologies, it is difficult to say with certainty what caused these sharp textural features in the irradiated sample. The possibility that He^{2+} irradiation contributed either fully or partly to the formation of these zones must likewise be considered. There are similarities between the features seen here and with He bubble formation observed in glass implanted with He^{2+} ions [44], and with voids caused by the accumulation of irradiation induced vacancies seen in ceramics [45]. In-situ observation of void formation in ceramics saw agglomeration and migration of these features towards grain boundaries [45]. Given the sharp textural break observed in Fig. 8B, void formation is considered a possibility; but as previously stated, the mechanism of formation cannot be stated with certainty from this analysis. To better clarify the contributions of the He^{2+} irradiation impact, in situ irradiation with concurrent TEM observation would be required to allow the differentiation of preparation artefacts from the ion implantation effects.

EDX mapping of the TEM lamella was completed to assess whether any chemical zonation occurred as a result of the He^{2+} irradiation. The results support the findings of the point TEM EDX analysis and additional SEM EDX (Appendix A) analysis. No observable banding was seen in CEM4M or CEM3Y, which are shown in Figs. 9 and 10, respectively.

EDX analysis was completed throughout the irradiated and control samples. The CEM3Y control FIB sample contained a smaller area of electron transparency than the He^{2+} sample purely because of unreacted BFS content that was invisible when sample area selection was completed. Also, when the stage was tilted to allow EDX analysis, some of the sample was obscured, further reducing the available area for analysis. This resulted in fewer points being analysed for the control sample.

The overall Ca/Si ratios for irradiated and control samples appear similar, as shown in Figs. 11 and 12. The increased proportion of microcrystals in CEM4M led to increased data scatter, and the average C-S-H Ca/Si ratios of 1.17 ± 0.08 for the irradiated sample and 1.36 ± 0.13

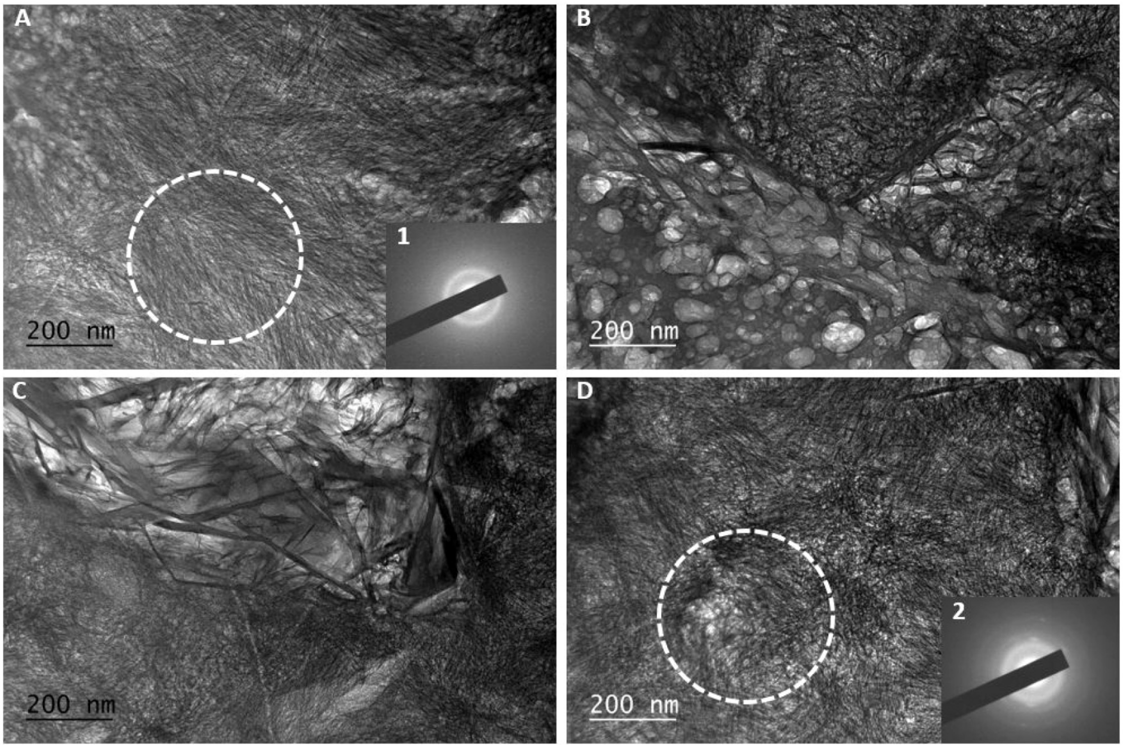

Fig. 8. TEM micrographs of CEM3Y He^{2+} irradiated. (A) <1 μm from the irradiated surface; the dashed circle represents the area of SAED pattern 1: C-S-H. (B) Approximately 2.8 μm from the irradiated surface with an interface between dense C-S-H foils and more open foils with many crystal lathes. (C) 4 μm from the irradiated surface with an interface of open foil-like C-S-H and dense foils. (D) >4 μm from the irradiated surface with dense fibrillar and foil-like C-S-H with zones of microcrystals; the dashed circle represents the area of SAED pattern 2: calcite.

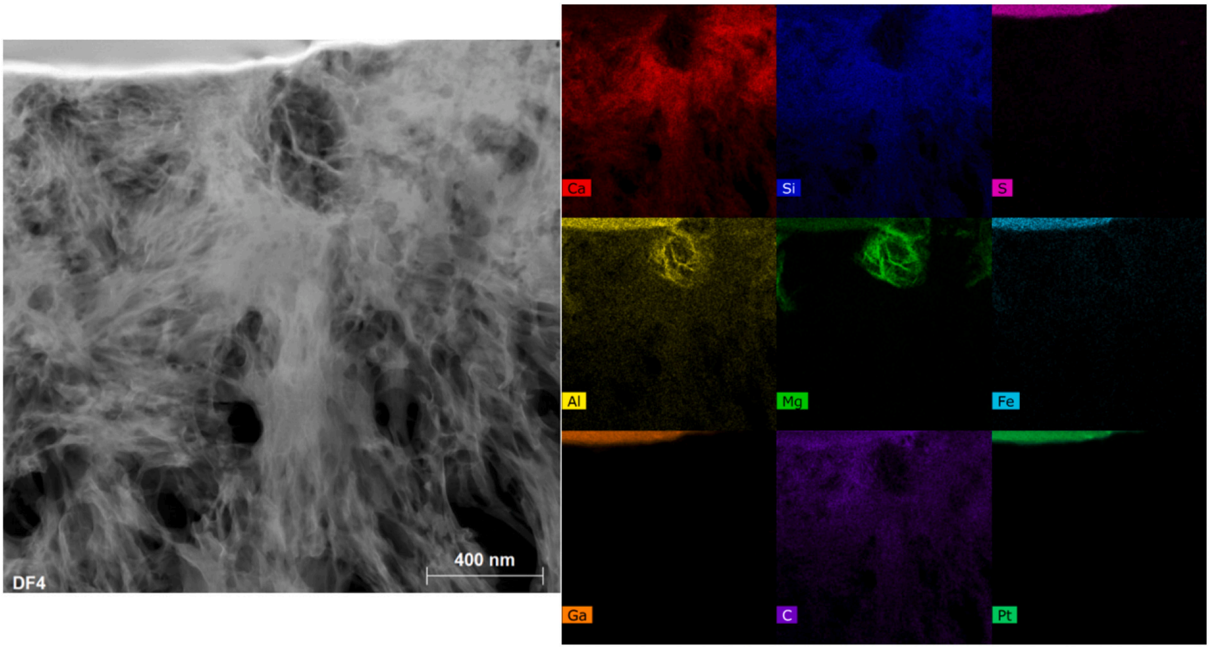

Fig. 9. EDX mapping of TEM lamella for the CEM4M He^{2+} sample. The irradiated surface is at the top of the image. Pt deposition and Ga are observed from the SEM-FIB preparation.

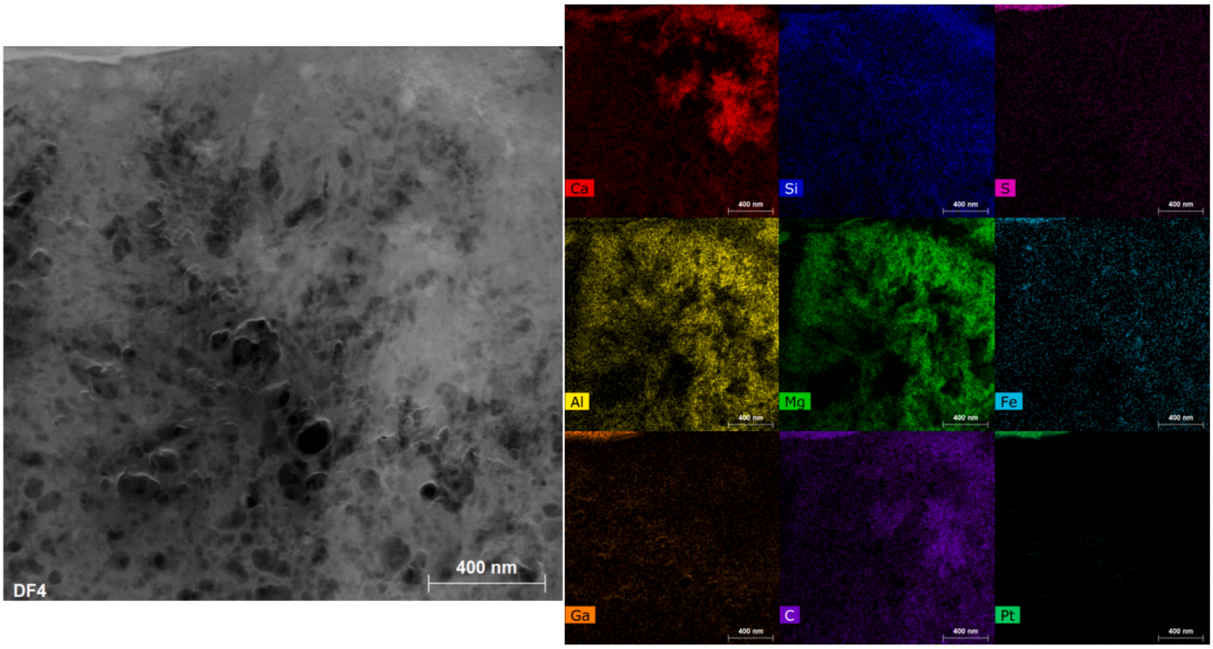

Fig. 10. EDX mapping of TEM lamella for the CEM3Y He^{2+} sample. The irradiated surface is at the top of the image. Pt deposition and Ga are observed from the SEM-FIB preparation.

and for the control sample also reflect this. An assessment of the Ca/Si ratio in the CEM4M control sample, excluding zones of microcrystals, produced a Ca/Si ratio of 1.04 ± 0.08. As outlined previously, the presence of microcrystals is not considered to be a product of irradiation exposure. Average Ca/Si ratios in CEM3Y were 1.21 ± 0.05 for the irradiated sample and 1.13 ± 0.07 for the control sample, indicating that there was limited bulk chemical response to irradiation. However, these data apply to averages across the samples that are inherently problematic because large variations in local composition are known to occur in cements of this type [46], particularly considering the presence of Calumite as part of the BFS fraction, which contains particles up to several hundred micrometres in size. Nevertheless, for the assessment of bulk properties, these figures are relevant and are similar to values previously stated in the literature for BFS:PC cements [33,46].

To assess whether the He^{2+} affected the various C-S-H morphologies differently, the areas identified as the inner and outer product were assessed. These areas were differentiated via textural identification and Mg/Si ratio assessment. Hydrotalcite is the only Mg-containing phase identified, and laths were identified within inner product zones or on textural boundaries, so this was considered a suitable proxy [46,47]. This segregation is shown in Figs. 11 and 12 in which the points considered to be the inner product show a much higher Al/Ca ratio. This

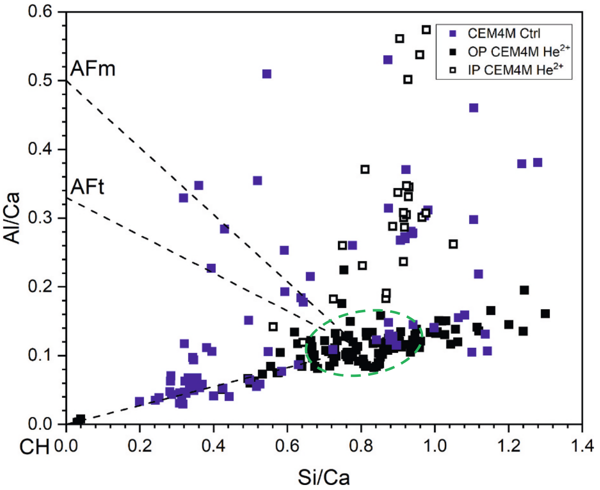

Fig. 11. EDX point analysis of CEM4M He^{2+} irradiated and control samples. The green dashed oval denotes the approximate C-A-S-H composition. Tie lines link to the other prominent hydrate phases: CH (portlandite); AFm (calcium monosulfoaluminate and monocarboaluminate); AFt (ettringite). (For interpretation of the references to colour in this figure legend, the reader is referred to the web version of this article.)

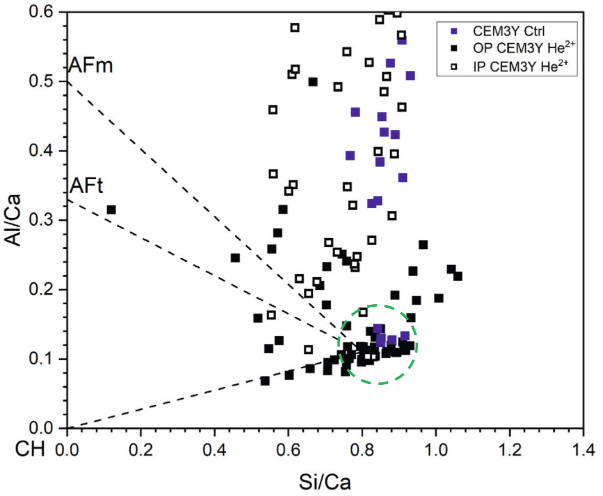

Fig. 12. EDX point analysis of CEM3Y He^{2+} irradiated and control samples. The green dashed circle denotes the approximate C-A-S-H composition. Tie lines link to the other prominent hydrate phases: CH (portlandite); AFm (calcium monosulfoaluminate and monocarboaluminate); AFt (ettringite). (For interpretation of the references to colour in this figure legend, the reader is referred to the web version of this article.)

is expected given the criteria used for identification because hydrotalcite is also rich in Al.

In both samples, the overall range of Ca/Si values was similar for inner and outer product regions, which was expected based on previous work on these cements [33,46]. However, a minor decrease in the average value for the outer product was observed; this was greater in the CEM4M sample, which was due to the lower Ca content in C-S-H observed in areas with no microcrystals. In CEM3Y, this shift is a product of the level of intermixing from hydrotalcite, which likely masks any other changes in the Ca/Si ratio that might have occurred. Despite the increased resolution provided by TEM analysis, the hydrotalcite laths are too small and pervasively intermixed with the C-S-H matrix in the inner product to be separately analysed.

The relationship between Mg/Si and Al/Si molar ratios in each sample is shown in Figs. 13 and 14. There is clear confirmation of a Mg-rich hydrotalcite-like phase present within the irradiated and control samples, which supports the XRD findings. The data correlate broadly with the tie line to a quintinite-like composition ($Mg_4Al_2(OH)_{12}CO_3{\cdot}4H_2O$) containing an Mg/Al ratio of 2, although it tracks slightly below this value, indicating estimated true values of 1.8–1.9, which is comparable with values previously determined in similar formulations [33]. These values are lower than the minimum value required for hydrotalcite-type phase formation, which has been attributed to the interstratification of $Al(OH)_3$ layers within the phase [39,48].

In CEM4M, there is clear localisation of the Mg/Al-rich phase in the inner product with negligible data from the control sample and outer product zones. This is expected given the age of this sample. However, a comparison between regions of the inner and outer product in CEM3Y indicates that some outer product zones also contain the Mg-rich hydrotalcite-like phase. The slightly higher Al content within the inner product is due to the initial differences in local chemistry rather than irradiation exposure [46]. The assessment here indicates that exposure to He^{2+} irradiation does not cause significant variation in the Mg/Al

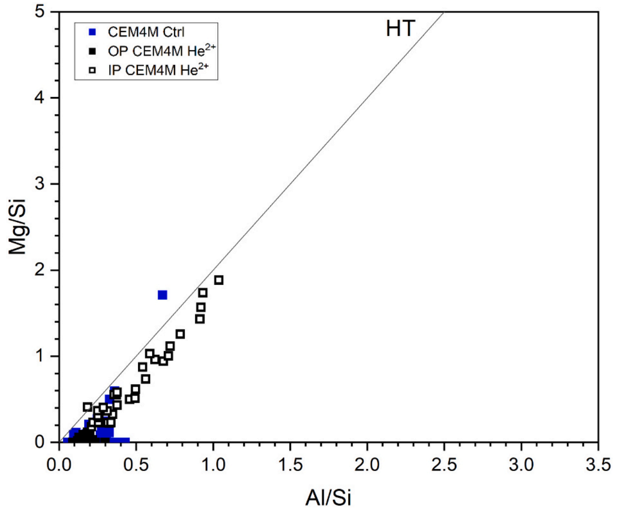

Fig. 13. Mg/Si and Al/Si atomic plots from the EDX point analysis of CEM4M He^{2+} irradiated and control samples. The HT tie line links to an idealised hydrotalcite-like composition with Mg/Al = 2.

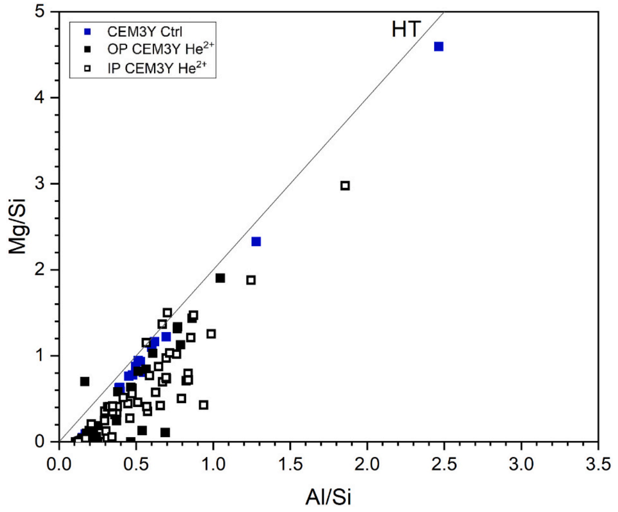

Fig. 14. Mg/Si and Al/Si atomic plots from the EDX point analysis of CEM3Y He^{2+} irradiated and control samples. The HT tie line links to an idealised hydrotalcite-like composition with Mg/Al = 2.

ratio, although further analysis of the control sample is required to have complete confidence in this statement.

Although monosulfoaluminate was identified from the XRD results, no clear indication of this phase was observed within the microstructure of the samples. An assessment of the EDX data showed that very low S/Ca ratios were present within the control sample (S/Ca <0.02) with slightly increased mean values in the irradiated sample (S/Ca <0.06), but no significant S concentrations were observed. This indicates that there was only a small amount of intermixed monosulfoaluminate within the C-S-H that underwent analysis. Given the large amount of inner product associated with BFS identified in these samples, it is unsurprising that such low S/Ca ratios were observed. Nevertheless, He^{2+} exposure appears to not have caused redox changes in the sulfide species from the BFS that were previously postulated to cause later-age ettringite formation [49].

4. Conclusions

The experimental setup outlined here provides a proof of concept for ion accelerator use to simulate alpha particle damage in cementitious materials. Sample heating was successfully minimised; although minor cracking was observed on the surface of the He^{2+} sample, this might have been a product of the vacuum rather than the heating effects. The phase assemblage preservation appeared successful when compared with the control samples. This is valuable for future experimental work investigating the long-term aging of cement materials used for waste form purposes and in the construction of long-term disposal facilities for radioactive waste.

He^{2+} irradiation induced a colour change in the cement sample surface was found to be similar to the discolouration observed in radiohaloes. The cause of this is currently unknown because no evidence of ballistic damage was observed from XRD analysis, but an analysis of the alterations to oxidation states could provide the information needed to clarify the mechanism responsible for the colour change.

Minor increased carbonation was observed in a 3-year cured sample (CEM3Y) through XRD and FTIR, potentially supporting the radiolytic production of CaO_2 octahydrate due to He^{2+} exposure. This was not observed in the 4-month cured sample CEM4M, where the control sample was more heavily carbonated. Given the younger age of CEM4M, the reduced Ca availability caused by a lower degree of hydration might have inhibited the radiolytic production of $CaO_2{\cdot}8H_2O$. This minor increase in CEM3Y was not observed to manifest in microscopic investigation, and no increased microcrystalline zonation was seen from SAED data collected in the damaged region. However, because atmospheric carbonation was not controlled during this experiment, this cannot be stated with certainty.

Microstructural and chemical investigations via TEM EDX and SEM EDX (Appendix A) showed no textural or chemical distinctions between the estimated damage zone and the pristine bulk/control sample. The irradiated sample surface appeared slightly rougher than the control; however, this could be a product of water loss due to irradiation, which was shown in the FTIR results. Despite the overall similarities between the control and irradiated samples, some regions of damaged microstructure were observed in the CEM3Y He^{2+} irradiated sample. The cause of these features cannot be assigned with certainty because, although beam damage from SEM FIB or TEM might be responsible, it might represent He^{2+} damage. To effectively resolve this, in situ irradiation with concurrent TEM observation would be required to allow for the differentiation of artefact preparation from the ion implantation effects.

The minor variations observed from this study pose interesting avenues for future investigations, although the impact of these differences on the ability of the cement to perform as a wasteform material is considered limited.

Declaration of competing interest

The authors declare that they have no known competing financial interests or personal relationships that could have appeared to influence the work reported in this paper.

Acknowledgements

The authors wish to acknowledge the Engineering and Physical Sciences Research Council, which funded the research activity performed by the University of Sheffield via the Next Generation Nuclear Centre for Doctoral Training. This research was performed in part at the MIDAS Facility at the University of Sheffield, which was established with support from the UK Department of Energy and Climate Change. Part of this work was supported by the US Department of Energy's (DOE's) Office of Nuclear Energy under DOE Idaho Operations Office Contract DE-AC07-051D14517 as part of a Nuclear Science User Facilities experiment. Parts of this research were carried out at IBC at the Helmholtz-Zentrum Dresden - Rossendorf e. V., a member of the Helmholtz Association. We would like to thank Dr. Shavkat Akhmadaliev for assistance with, and for performing, the He^{2+} irradiations.

Appendix A. Supplementary data

Supplementary data to this article can be found online at https://doi.org/10.1016/j.cemconres.2022.106895.

References

[1] Nuclear Decommissioning Authority, Waste Stream 2D22: Magnox Cladding and Miscellaneous Solid Waste, 2013.

[2] Radioactive Waste Management, Geological disposal: guidance on the production of encapsulated wasteforms, in: NDA Report WPS/502/01, RWM-NDA, Didcot, UK, 2015.

[3] Nuclear Decommissioning Authority, Waste package specification and guidance documentation, WPS/800: wasteform specification for 500 litre drum waste package: explanatory material and design guidelines, in: NDA Report 9699292, NDA, Didcot, UK, 2008.

[4] W.R. Bower, C.I. Pearce, G.T.R. Droop, J.F.W. Mosselmans, K. Geraki, R.A. D. Pattrick, Radiation damage from long-term alpha particle bombardment of silicates – a microfocus XRD and Fe K -edge XANES study, Mineral. Mag. 79 (2015) 1455–1466, https://doi.org/10.1180/minmag.2015.079.6.20.

[5] S. Curwen, M.J. Angus, Review of hydraulic cements for plutonium encapsulation, in: Nexia Solutions Report (07) 8903, Risley, UK, 2007.

[6] S.A. Kearney, B. McLuckie, K. Webb, R. Orr, I.A. Vatter, A.S. Yorkshire, C. L. Corkhill, M. Hayes, M.J. Angus, J.L. Provis, Effects of plutonium dioxide encapsulation on the physico-chemical development of Portland cement blended grouts, J. Nucl. Mater. 530 (2020), 151960, https://doi.org/10.1016/j.jnucmat.2019.151960.

[7] Radioactive Waste Management, Geological disposal, RWM HAW innovation and delivery: a review of cement powders security of supply, specifications and disposability issues, in: NDA Report Number NDA/RWM/144, RWM-NDA, Didcot, UK, 2016.

[8] G.R. Choppin, J.-O. Liljenzin, J. Rydberg, Chapter 4 – unstable nuclei and radioactive decay, in: Radiochemistry and Nuclear Chemistry, Third Edition, Elsevier Butterworth Heinemann, Oxford, UK, 2002, pp. 58–93, https://doi.org/10.1016/B978-075067463-8/50004-2.

[9] Health Physics Society, Human health fact sheet, Plutonium, Argonne National Laboratory, Argonne IL, 2001. https://remm.hhs.gov/ANL_ContaminantFactSheets_All_070418.pdf.

[10] Health Physics Society, Human health fact sheet, Uranium, Argonne National Laboratory, Argonne IL, 2001. https://remm.hhs.gov/ANL_ContaminantFactSheets_All_070418.pdf.

[11] J.F. Ziegler, M.D. Ziegler, J.P. Biersack, SRIM - the stopping and range of ions in matter (2010), Nucl. Instr. Meth. Phys. Res. Sect. B 268 (2010) 1818–1823, https://doi.org/10.1016/j.nimb.2010.02.091.

[12] R.C. Ewing, W.J. Weber, J. Lian, Nuclear waste disposal-pyrochlore ($A_2B_2O_7$): nuclear waste form for the immobilization of plutonium and “minor” actinides, J. Appl. Phys. 95 (2004) 5949–5971, https://doi.org/10.1063/1.1707213.

[13] T. Allard, J.P. Muller, J.C. Dran, M.T. Ménager, Radiation-induced paramagnetic defects in natural kaolinites: alpha dosimetry with ion beam irradiation, Phys. Chem. Miner. 21 (1994) 85–96, https://doi.org/10.1007/BF00205219.

[14] W.R. Bower, C.I. Pearce, A.D. Smith, S.J. Plimbott, J.F.W. Mosselmans, S.J. Haigh, J.P. Mckinley, R.A.D. Patrick, Radiation damage in biotite mica by accelerated α-particles : a synchrotron microfocus X-ray diffraction and X-ray absorption spectroscopy study, Am. Mineral. 101 (2016) 928–942, https://doi.org/10.2138/am-2016-5280CCBYNCND.

[15] C.A. Taylor, M.K. Patel, J.A. Aguiar, Y. Zhang, M.L. Crespillo, J. Wen, H. Xue, Y. Wang, W.J. Weber, Bubble formation and lattice parameter changes resulting from He irradiation of defect-fluorite $Gd_2Zr_2O_7$, Acta Mater. 115 (2016) 115–122, https://doi.org/10.1016/j.actamat.2016.05.045.
[16] L. Nasdala, D. Grambole, J. Götze, U. Kempe, T. Váczi, Helium irradiation study on zircon, Contrib. Mineral. Petrol. 161 (2011) 777–789, https://doi.org/10.1007/s00410-010-0562-7.
[17] K.L. Scrivener, A. Bazzoni, B. Mota, J.E. Rossen, Electron microscopy, in: K. L. Scrivener, R. Snellings, B. Lothenbach (Eds.), A Practical Guide to Microstructural Analysis of Cementitious Materials, CRC Press, Boca Raton, 2016, pp. 353–416, https://doi.org/10.1007/978-1-62703-776-1.
[18] D.P. Prentice, B. Walkley, S.A. Bernal, M. Bankhead, M. Hayes, J.L. Provis, Thermodynamic modelling of BFS-PC cements under temperature conditions relevant to the geological disposal of nuclear wastes, Cem. Concr. Res. 119 (2019) 21–35, https://doi.org/10.1016/j.cemconres.2019.02.005.
[19] W.R. Bower, R.A.D. Pattrick, C.I. Pearce, G.T.R. Droop, S.J. Haigh, Radiation damage haloes in biotite investigated using high-resolution transmission electron microscopy, Am. Mineral. 101 (2016) 105–110, https://doi.org/10.2138/am-2016-5349CCBY.
[20] A.M. Seydoux-Guillaume, R. Wirth, L. Nasdala, M. Gottschalk, J.M. Montel, W. Heinrich, An XRD, TEM and raman study of experimentally annealed natural monazite, Phys. Chem. Miner. 29 (2002) 240–253, https://doi.org/10.1007/s00269-001-0232-4.
[21] D.C. Pal, T. Chaudhuri, Radiation damage-controlled localization of alteration haloes in albite: implications for alteration types and patterns Vis-à-Vis mineralization and element mobilization, Mineral. Petrol. 110 (2016) 823–843, https://doi.org/10.1007/s00710-016-0453-3.
[22] P. Barnes, J. Bensted, Structure and Performance of Cements, 2nd Edition, Spon Press, Taylor and Francis Group, London, UK, 2008, https://doi.org/10.1201/9781482295016.
[23] N.B.A. Thompson, S.E. O'Sullivan, R.J. Howell, D.B. Bailey, M.G. Gilbert, N. C. Hyatt, Objective colour analysis from digital images as a nuclear forensic tool, Forensic Sci. Int. 319 (2021), 110678.
[24] L. Nasdala, M. Wildner, R. Wirth, N. Groschopf, D.C. Pal, A. Möller, Alpha particle haloes in chlorite and cordierite, Mineral. Petrol. 86 (2006) 1–27, https://doi.org/10.1007/s00710-005-0104-6.
[25] L. Nasdala, M. Wenzel, M. Andrut, R. Wirth, P. Blaum, The nature of radiohaloes in biotite: experimental studies and modeling, Am. Mineral. 86 (2001) 498–512, https://doi.org/10.2138/am-2001-0414.
[26] R.A.D. Pattrick, J.M. Charnock, T. Geraki, J.F.W. Mosselmans, C.I. Pearce, S. Pimblott, G.T.R. Droop, Alpha particle damage in biotite characterized by microfocus X-ray diffraction and FeK-edge X-ray absorption spectroscopy, Mineral. Mag. 77 (2013) 2867–2882, https://doi.org/10.1180/minmag.2013.077.6.12.
[27] M. Chaouche, X.X. Gao, M. Cyr, M. Cotte, L. Frouin, On the origin of the blue/green color of blast-furnace slag-based materials: sulfur K-edge XANES investigation, J. Am. Ceram. Soc. 100 (2017) 1707–1716, https://doi.org/10.1111/jace.14670.
[28] R. Steudel, T. Chivers, The role of polysulfide dianions and radical anions in the chemical, physical and biological sciences, including sulfur-based batteries, Chem. Soc. Rev. 48 (2019) 3279–3319, https://doi.org/10.1039/c8cs00826d.
[29] M. Levy, J.H.O. Varley, Radiation induced colour centres in fused quartz, Proc. Phys. Soc. Sect. B. 68 (1955) 223–233, https://doi.org/10.1088/0370-1301/68/4/304.
[30] G.L.C. De Lima, F.S. Lameiras, Color change of gemstones by exposure to gamma rays, in: International Nuclear Atlantic Conference (INAC) 2015 Conference Proceedings, São Paulo, Brazil, Associação Brasileira de Energia Nuclear, 2015.
[31] M.R. Krbetschek, J. Götze, A. Dietrich, T. Trautmann, Spectral information from minerals relevant for luminescence dating, Radiat. Meas. 27 (1997) 695–748, https://doi.org/10.1016/S1350-4487(97)00223-0.
[32] D.P. Prentice, S.A. Bernal, M. Bankhead, M. Hayes, J.L. Provis, Phase evolution of slag-rich cementitious grouts for immobilisation of nuclear wastes: an experimental and modelling approach, Adv. Cem. Res. 30 (2018) 345–360, https://doi.org/10.1680/jadcr.17.00198.
[33] R. Taylor, I.G. Richardson, R.M.D. Brydson, Composition and microstructure of 20-year-old ordinary Portland cement-ground granulated blast-furnace slag blends containing 0 to 100% slag, Cem. Concr. Res. 40 (2010) 971–983, https://doi.org/10.1016/j.cemconres.2010.02.012.
[34] P. Yu, R.J. Kirkpatrick, B. Poe, P.F. McMillan, X. Cong, Structure of calcium silicate hydrate (C-S-H): near-, mid-, and far-infrared spectroscopy, J. Am. Ceram. Soc. 82 (1999) 742–748, https://doi.org/10.1111/j.1151-2916.1999.tb01826.x.
[35] F.A. Andersen, L. Brečević, Infrared spectra of amorphous and crystalline calcium carbonate, Acta Chem. Scand. 45 (1991) 1018–1024, https://doi.org/10.3891/acta.chem.scand.45-1018.
[36] P. Bouniol, A. Aspart, Disappearance of oxygen in concrete under irradiation: the role of peroxides in radiolysis, Cem. Concr. Res. 28 (1998) 1669–1681, https://doi.org/10.1016/S0008-8846(98)00138-0.
[37] I. Maruyama, S. Ishikawa, J. Yasukouchi, S. Sawada, R. Kurihara, M. Takizawa, O. Kontani, Impact of gamma-ray irradiation on hardened white Portland cement pastes exposed to atmosphere, Cem. Concr. Res. 108 (2018) 59–71, https://doi.org/10.1016/j.cemconres.2018.03.005.
[38] F. Vodák, V. Vydra, K. Trtík, O. Kapičková, Effect of gamma irradiation on properties of hardened cement paste, Mater. Struct. 44 (2011) 101–107, https://doi.org/10.1617/s11527-010-9612-x.
[39] R. Taylor, I.G. Richardson, R.M.D. Brydson, Nature of C-S–H in 20 year old neat ordinary Portland cement and 10% Portland cement–90% ground granulated blast furnace slag pastes, Adv. Appl. Ceram. 106 (2007) 294–301, https://doi.org/10.1179/174367607X228106.
[40] K.L. Scrivener, A. Nonat, Hydration of cementitious materials, present and future, Cem. Concr. Res. 41 (2011) 651–665, https://doi.org/10.1016/j.cemconres.2011.03.026.
[41] E. Tajuelo Rodriguez, W.A. Hunnicutt, P. Mondal, Y. Le Pape, Examination of gamma irradiated calcium silicate hydrates. Part I: chemical-structural properties, J. Am. Ceram. Soc. 103 (2020) 558–568, https://doi.org/10.1111/jace.16515.
[42] J.D. Arregui-Mena, P.D. Edmondson, A.A. Campbell, Y. Katoh, Site specific, high-resolution characterisation of porosity in graphite using FIB-SEM tomography, J. Nucl. Mater. 511 (2018) 164–173, https://doi.org/10.1016/j.jnucmat.2018.08.047.
[43] S. Kelly, H. El-Sobky, C. Torres-Verdín, M.T. Balhoff, Assessing the utility of FIB-SEM images for shale digital rock physics, Adv. Water Resour. 95 (2016) 302–316, https://doi.org/10.1016/j.advwatres.2015.06.010.
[44] G. Gutierrez, S. Peuget, J.A. Hinks, G. Greaves, S.E. Donnelly, E. Oliviero, C. Jégou, Helium bubble formation in nuclear glass by in-situ TEM ion implantation, J. Nucl. Mater. 452 (2014) 565–568, https://doi.org/10.1016/j.jnucmat.2014.06.010.
[45] S.M. Lawson, G. Greaves, L.R. Blackburn, R. Chapman, N.C. Hyatt, C.L. Corkhill, Synthesis and in situ ion irradiation of A-site deficient zirconate perovskite ceramics, J. Mater. Chem. A 8 (2020) 19454–19466, https://doi.org/10.1039/d0ta05255h.
[46] I.G. Richardson, G.W. Groves, Microstructure and microanalysis of hardened cement pastes involving ground granulated blast-furnace slag, J. Mater. Sci. 27 (1992) 6204–6212, https://doi.org/10.1007/BF01133772.
[47] H.F.W. Taylor, Cement Chemistry, 2nd Edition, UK, Thomas Telford Publishing, London, 1997.
[48] G.W. Brindley, S. Kikkawa, A crystal-chemical study of Mg,Al and Ni,Al hydroxy-perchlorates and hydroxy-carbonates, Am. Mineral. 64 (1979) 836–843.
[49] I.G. Richardson, G.W. Groves, C.R. Wilding, Effect of gamma radiation on the microstructure and microchemistry of GGBFS/OPC cement blends, MRS Symp. Proc. 176 (1990) 31–37.